PNAS RESEARCH ARTICLE | APPLIED PHYSICAL SCIENCES OPEN ACCESS

Coupling between electrons' spin and proton transfer in chiral biological crystals

Naama Goren[a], Perumal Pandurangan[b,1], Yael Eisenberg-Domovich[c], Shira Yochelis[a], Nir Keren[d], Jean-Philippe Ansermet[e], Ron Naaman[f,2], Oded Livnah[c], Nurit Ashkenasy[b,2], and Yossi Paltiel[a,2]

Affiliations are included on p. 7.

Edited by Monica Olvera de la Cruz, Northwestern University, Evanston, IL; received January 10, 2025; accepted April 3, 2025

Proton transport plays a fundamental role in many biological and chemical systems. In life, proton transport is crucial for biochemical and physiological functions. It is usually accepted that the main mechanism of proton transfer is a result of hopping between neighboring water molecules and amino acid side chains. It was recently suggested that the proton transfer can be simultaneously coupled with electron transfer. As life is homochiral, proton transfer in biology is occurring in a chiral environment. In this environment, the chiral-induced spin selectivity effect relating to electron transfer and chirality is expected to occur. The present work establishes that the proton transfer is coupled to a specific electron spin polarization in lysozyme crystals, associating proton transfer to electron movement and polarization. To preserve total angular momentum, this motion may be coupled to chiral phonons that propagate in the crystal. Our work shows that the interaction of the electrons' spin and phonons is very significant in proton transfer through lysosome crystals. Injecting the opposite electron spin into the lysosome crystal results in a significant change in proton transfer impedance. This study presents the support for the proton-coupled electron transfer mechanism and indicates the importance of spin polarization in the process.

the CISS effect | proton-transfer | proton-coupled electron transfer (PCET) | lysozyme crystals

Proton transport is crucial in diverse biochemical and physiological functions of living organisms (1, 2). This process is essential for cellular respiration, photosynthesis, and the maintenance of intercellular electrochemical gradients, among other critical functions (3). It is facilitated by various proteins and complexes, including proton pumps, channels, and molecular carriers, which ensure the efficient movement of protons across biological membranes (4–6). For instance, the proton pump adenosine triphosphate (ATP) synthase in mitochondria and chloroplasts is vital for ATP production (1, 7).

Within proton transfer pathways of pumps and channels, interactions with amino acids play pivotal roles (8). The protonation and deprotonation of these amino acids are tuned by the surrounding protein environment, which stabilizes transition states and lowers the activation energy for proton transfer (6, 9, 10). In many of these systems, protons move through a medium by hopping between neighboring water molecules or other suitable molecular carriers. This mechanism relies on the ability of protons to exchange positions or charge with hydrogen atoms in the surrounding environment, facilitated by the presence of water or specific proton-conducting materials (11, 12).

It is important to note that proton hopping is accompanied by changes in the electron distribution in its vicinity, generating an electric polarization (11, 13). This polarization is enhanced by vibrations—phonons, and hence the proton transfer is facilitated by phonon-assisted jumps (14–16). The activation energy for these jumps is determined by the frequencies of the phonons, meaning that specific phonon modes can influence the extent of proton motion (14, 17–19).

In recent years, proton transfer is considered to be coupled to a electron transfer (PCET) mechanism (20, 21). This process involves the transfer of electrons and protons from one atom to another (22). It is important to note that in chiral systems, this electron polarization is generated in the chiral environment.

It was shown that chirality is related to electron spin and angular momentum preservation through the chiral-induced spin selectivity (CISS) effect (23). Within the CISS effect, an electron has a preferred spin state upon motion through a chiral structure (24). Since life is homochiral, electron transfer in biology is occurring in homochiral environments and is susceptible to CISS effects. Combining the PCET mechanism and the CISS effect should result in spin-related proton transport.

Also, in chiral structures, one chirality of the phonons is preferred. Chiral phonons have angular momentum, and in chiral structures, they produce a magnetic field (25, 26). These

Significance

This research uncovers a groundbreaking link between electron spin and proton transport in biological environment, using lysozyme as a model system. Proton transfer, vital in many life processes, is shown to couple with electron spin polarization, a discovery aligned with the Chiral Induced Spin Selectivity (CISS) effect. Specifically, we show that proton conduction through the lysozyme crystal is selective to the polarization of injected electrons, highlighting a synergy between spin polarization and information transfer in life. This mechanism provides insights into proton-coupled electron transfer (PCET) processes, emphasizing the role of chirality in biological processes. These findings bridge quantum physics with biochemistry enabling better understanding and opening the possibility of controlled information transfer in biological environments.

The authors declare no competing interest.

This article is a PNAS Direct Submission.

[1]Present address: Department of Hydro and Electrometallurgy, Council of Scientific & Industrial Research Institute of Minerals and Materials Technology, Bhubaneswar, Odisha 750103, India.

[2]To whom correspondence may be addressed. Email: ron.naaman@weizmann.ac.il, nurita@bgu.ac.il, or paltiel@mail.huji.ac.il.

This article contains supporting information online at https://www.pnas.org/lookup/suppl/doi:10.1073/pnas.2500584122/-/DCSupplemental.

Published May 8, 2025.

phonons can have unique effects on electronic and thermal transport properties, including modulating electron–phonon interactions and inducing topologically protected states. Chiral phonons are embedded in the basic mechanism of the CISS effect by the connection between spin, nuclear motion, and electronic structure (27–30).

While the influence of the CISS effect on electron transport has been extensively studied in the context of electron conductivity (31–33), its implications for proton conduction remain unexplored. In this work, we probe the efficiency of proton transport processes through proteins. We use Hen egg white lysozyme crystals that tend to crystallize easily in a tetragonal space group symmetry as a model system (34). Lysozyme, a well-known and extensively studied glycoside hydrolase enzyme, originates from various biological sources, including egg whites and human tears, saliva, and mucus (35). Such crystals were recently used as a chiral environment to demonstrate an electronic CISS effect in carbon nanotubes (36).

The electric properties of the chiral lysozyme crystals have been widely investigated (37–40) due to their significance in various biological processes, such as the protection from bacterial infections (41). Lysozyme's dominant charge carrier are protons (37, 38); its conductivity is controlled by proton transfer at humidity above 10% (38). The conductivity drops dramatically at low humidity when proton transfer is reduced to a residual electron conductance that is orders of magnitude smaller (38). At very high humidity levels (above 60%), the crystal structure becomes flexible, reducing the interactions of the crystal phonons with the proton current (42, 43).

Here, we demonstrate that the proton transfer process in Lysozyme crystals is coupled to electron transfer. By the injection of spin-polarized electrons into the crystal, we show a relations between the efficiency of proton transport in the biological crystals and the chirality of the crystal and of the electron spin. The proton transfer process is coupled with electron spin injection that induces excitation of chiral phonons. As a result, phonon excitation enhances the proton transfer in a spin-selective manner.

Results

Lysozyme crystals were grown by the hanging-drop vapor-diffusion method (44). A single crystal was positioned on a device consisting of Ni and Au electrodes spaced approximately 2 μm apart on a Si/SiO_2 substrate (Fig. 1). Details regarding the crystallization process and device fabrication are provided in the *Methods* section.

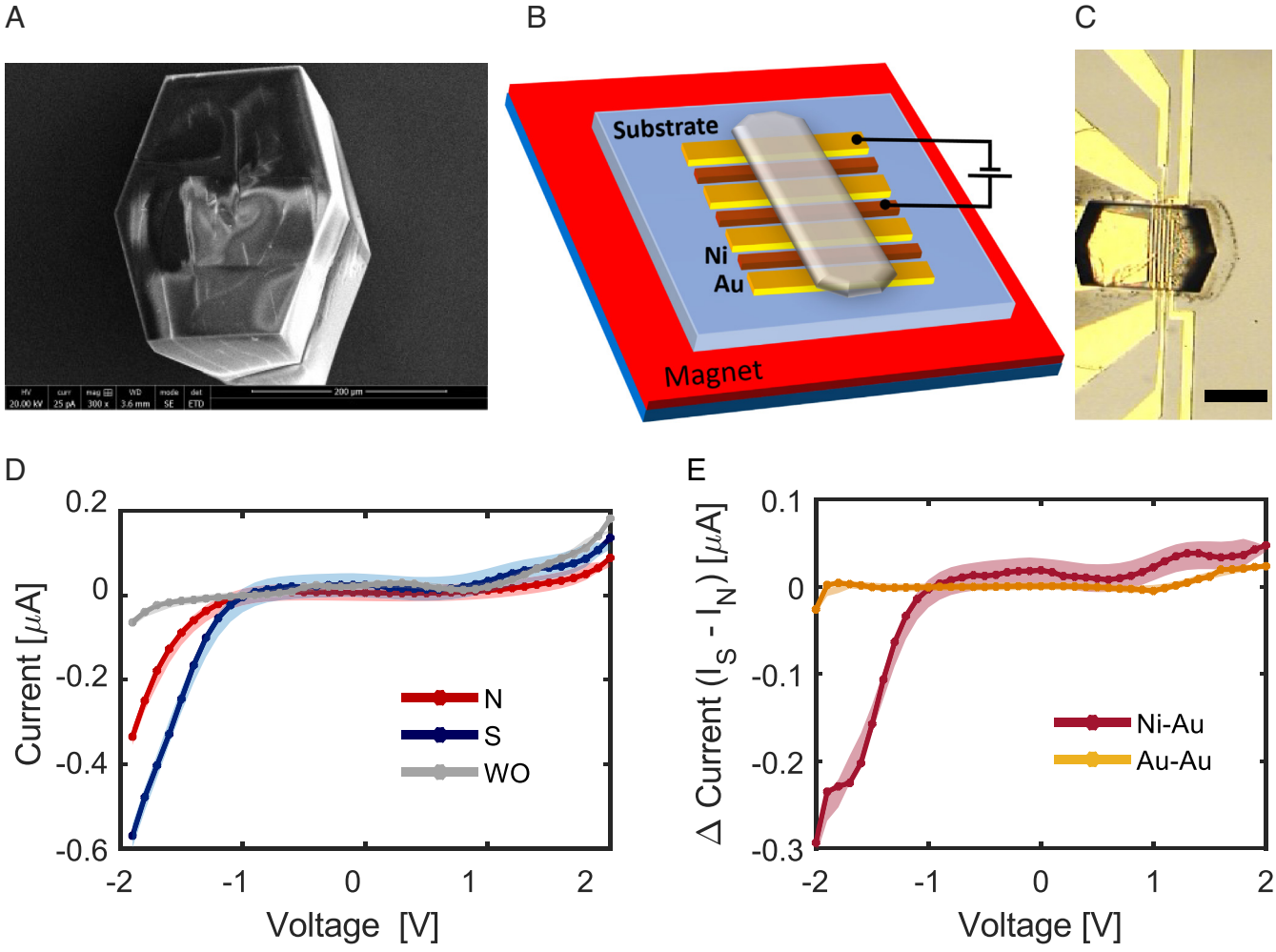

Fig. 1. Experimental setup and IV characterizations. (*A*) SEM image of a lysozyme crystal. More SEM images including dimension measurements can be found in *SI Appendix*, Fig. S1. (*B*) Schematic illustration of the device setup: The lysozyme crystal is positioned atop alternating Ni and Au electrodes electrically connected. A constant magnet is placed beneath the device, allowing to magnetize the Ni layer out-of-plane using the North (N) and South (S) poles, or leaving it unmagnetized by removing the magnet (WO). (*C*) Microscope image of the device, with a scale bar of 100 μm. (*D*) IV measurements using Ni–Au electrodes under S, N, and WO magnetizations, shaded area denotes the measurement error. Additional measurements from different crystals are presented in *SI Appendix*, Fig. S10. (*E*) The difference in the current in the S and N magnetizations extracted from IV measurements under different electrode configurations with fixed North pole magnetization. Measurements were conducted at 70% RH and a temperature of 23 °C, with each condition repeated 10 times; the shaded area denotes the measurement error. Additional measurements from different crystals are presented in *SI Appendix*, Fig. S11. A closer look at the small voltages under 1 V is presented in *SI Appendix*, Fig. S12. At low current, a nonlinear effect is measured, suggesting a secondary effect of the current. We will address this point later.

Representative images of the lysozyme crystal are shown in Fig. 1*A*. Fig. 1 *B* and *C* present a scheme and an optical micrograph of the device, respectively. Additional measured crystals are presented in *SI Appendix*, Fig. S7.

Investigating the interplay between electron spin and proton transport, current–voltage (IV), and impedance spectroscopy (IS) measurements were performed under varying environmental and magnetic conditions. The easy axis of the Ni electrode lies in-plane. A constant magnetic field of approximately 80 mT was applied using a fixed magnet positioned beneath the device, sufficient to saturate the Ni magnetization in one direction, toward the crystal (N), or away from the crystal (S).

Initial IV measurements were performed using the configuration shown in Fig. 1*B*, confirming adequate contact between the crystal and electrodes and providing a preliminary device characterization. During these measurements, the device was maintained in an environment of about 70% relative humidity (RH) and a temperature of 23C. A voltage sweep ranging from −2 V to 2 V was applied while recording the current response. All measurements were performed under identical ambient conditions, with minimal time between successive measurements to ensure consistency.

A difference in current was observed when the ferromagnetic Ni contact was magnetized either north or south, as compared to a nonmagnetized in-plane configuration (Fig. 1*D*). These results indicate that the conduction in the crystal, where protons serve as the primary conduction carriers (37, 38), is coupled with the electron spin of the electrode (45). This unexpected phenomenon, which links spin polarization to proton transport, is a core observation of this work and further addressed in the discussion section.

To confirm that the observed difference in the current between N and S magnetization originates from the magnetic contact, the Ni electrode was replaced with an Au electrode (Fig. 1*E*). In this Au–Au contacts configuration, the difference between the current measured with S and N polarization was diminished, verifying that the effect observed is due to the spin injection and not due to the magnetic field per se.

The proton conduction observed in the IV measurements could originate from water splitting occurring at the electrodes, which in return may be affected by the direction of magnetization (46, 47). To differentiate between the contribution of spin to proton conduction through the crystals and interfacial effects, IS measurements were carried out using a low voltage in a humidity-controlled environment and were chosen for its ability to probe the dynamic behavior of proton transport. More details on the setup and measurements are presented in the *Methods* section. To address the potential issue of water splitting at the electrodes, we note that DC measurements in *SI Appendix* were conducted under smaller voltages, well below the threshold for water splitting reactions. In these measurements, we also observed the CISS effect. It is also important to note that even if water splitting occurs, ions still need to move from one electrode to the other, meaning they must still be transported through the crystal.

Fig. 2*A* displays the Nyquist plots of a lysozyme crystal placed between two Ni contacts under the different magnetization states. The shape of the curve with a nonclosed semicircle appended by an inclined line is typical to proton-conducting materials (48, 49). The alteration of the radius of the semicircle with the magnetization of the nickel contacts clearly indicates that spin polarization of the contacts influences the transport of the protons through the crystal. The impedance spectra were analyzed using an equivalent circuit model consisting of R1 + (R2 || CPE) + CPE depicted at the *Inset* of Fig. 2*A*. In this model, R1 represents a negligible series resistance from the external measurement setup (The iDE resistance and the leads), R2 corresponds to the bulk resistance of the crystal, a constant phase element (CPE1) parallel to R2 indicates a nonideal capacitive behavior of the crystal, likely arising from space charge polarization, and CPE2 accounts for interfacial effects at the metal–crystal interface. This model was used to extract the relaxation time.

A typical bell-shaped loss tangent spectra was observed for the crystals, shifted in the frequency range depending on the magnetic polarization of the contacts (Fig. 2*B*), indicating that spin polarization induces a change in the charge carriers' relaxation time (48). Relaxation times of 13, 18, and 60 ms were extracted from the frequency of the maximal loss tangent value for the nonpolarized, N-polarized, and S polarized conditions, respectively. Similar results were obtained from a simplified fit of the Nyquist plot (*SI Appendix*, Fig. S2). The change in the carriers' relaxation time indicates that the proton mobility depends on the electrodes spin polarization with N polarization leading to three times larger mobility than the S polarization. It should be noted that the maximum value of the loss tangent did not change for the different polarization conditions, indicating that the charge carrier screening length (48), and hence their concentration, is not affected by the magnetization of the nickel contacts, as could be expected.

Fig. 3 *A*–*C* present several experiments in which IS measurements were used to validate the observed magnetization effects.

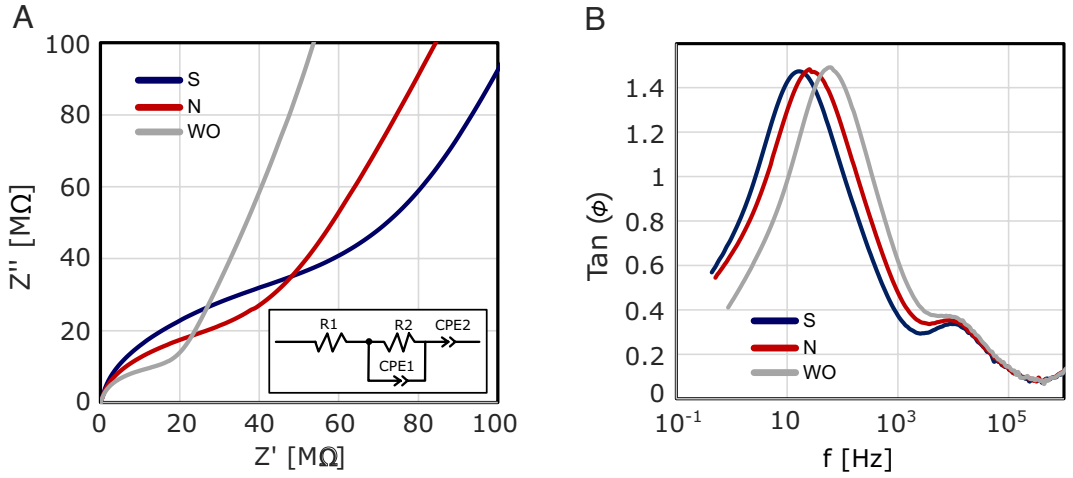

Fig. 2. IS of a single crystal of lysozyme placed between two nickel electrodes, under 60% RH and different polarizations. (*A*) Nyquist plot. *Inset* shows the equivalent circuit used to extract resistance values (R_2) for calculation of the %CISS in Fig. 3 *A*–*C*. (*B*) Loss tangent spectra of these measurements.

These experiments involved varying the RH, altering the connection configurations, and changing the hydrogen isotope of the humidity source. The percentage of the CISS effect, defined as $\%\,\mathrm{CISS} = 100 * \frac{R_N - R_S}{R_{S+R_N}}$ was calculated with R_N and R_S representing the resistances measured when the North and the South poles facing the crystal, respectively.

The dependence of the CISS effect on the contact composition is presented in Fig. 3*A*. The results show a significant difference between %CISS for Ni/Ni contacts and those with Au/Au contacts, similar to the results shown in Fig. 1*E*, obtained with DC measurements. The CISS effect was stronger with the ferromagnetic electrodes, suggesting that the observed behavior is related to the magnetization of the contacts. Transport measurements were performed under varying RH (60 to 80%). The typical decrease in the resistance of the crystal with increasing RH (*SI Appendix*, Fig. S3) was accompanied by a decrease in the CISS effect (Fig. 3*B*). Similar results were achieved for DC measurements as seen in *SI Appendix*, Fig. S4. This trend is consistent with the expected relaxation of the crystal structure at elevated humidity levels (42, 43). In higher humidity, the structure is less stiff. Additionally, at higher humidity, protons are more likely to transfer through water molecules rather than along the chiral crystal lattice, reducing their sensitivity to the crystal's chirality.

Measurements using D_2O instead of H_2O for humidification, presented in Fig. 3*C*, show likewise a reduction in the CISS effect when using D_2O. The higher resistance observed in the D_2O environment (*SI Appendix*, Fig. S8) is consistent with the involvement of proton transport, further supporting the role of proton mobility in the observed conduction mechanism (50, 51). The strongly suppressed dependence of conduction on spin polarization in the presence of D_2O may provide evidence of the role of phonons in the observed charge transfer process. This is because of the lower phonon energy in D_2O environment (52, 53), which diminishes electron polarization and subsequently weakens the CISS effect. In this scenario, the higher energy of the H_2O phonons can be coupled better with the large difference in energy between the transport of the two electron spin directions.

To probe the role of phonons in charge conduction, we measured the DC resistance of the device at various temperatures. The DC setup is the same as the configuration shown above (Fig. 1*B*), with the addition of a thermoelectric cooler pad to control the device's temperature. Measurements were performed while keeping the humidity at 70% RH. The CISS effect increased with temperature (Fig. 3*D*). This trend can be consistent with a phonon-based conduction mechanism, following many recent CISS-related studies (54). However, the overall reduction in conduction with temperature (*SI Appendix*, Fig. S5) suggests a reduction of the local humidity in the crystal at elevated temperatures that can also explain the increase in the CISS with increasing temperature.

To investigate further the connection between lattice vibrations and the induced polarization, second harmonic current measurements were performed while locally heating the sample using a 532 nm laser focused on one side of the crystal (Fig. 4*A*). The asymmetrical heating generates a nonsymmetric nonlinear response between the two sides of the crystal, measurable through second harmonic transport measurements (Fig. 4*B*). It is important to note that the second harmonic of the AC signal demonstrates that the response to an increase or a decrease in the applied voltage is not symmetric. This suggests a nonuniform flow along the crystal. Notably, the asymmetric response strongly depends on the injected spin, as seen in Fig. 4*C* where the changes in the

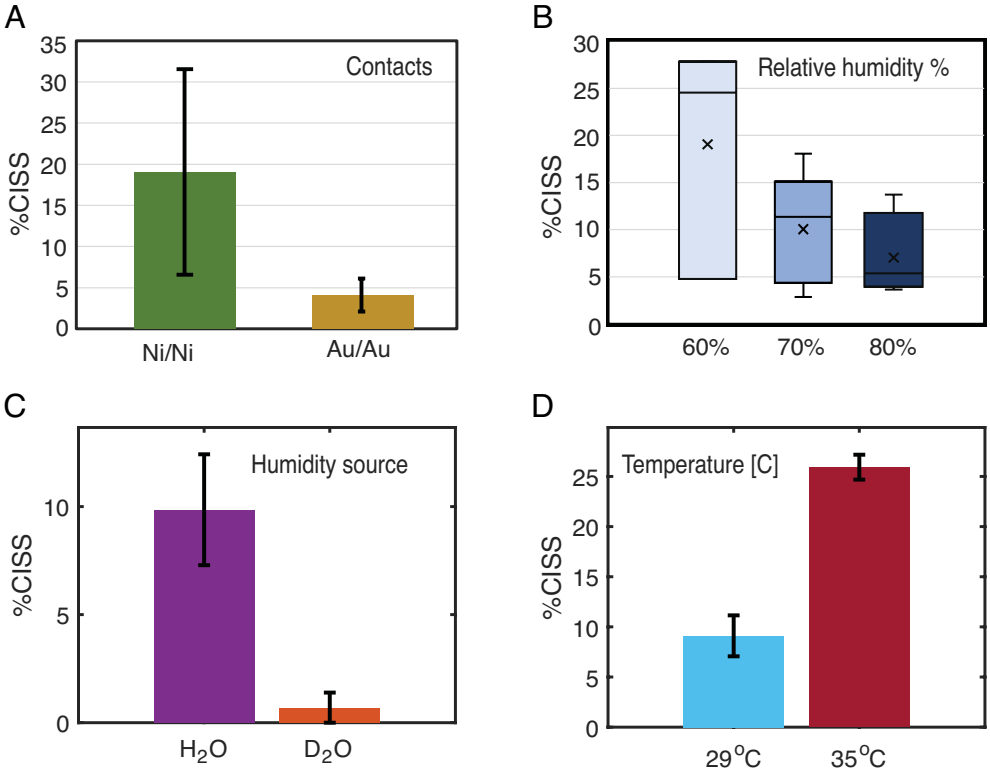

Fig. 3. The CISS effect under various conditions. %CISS is defined as $\%\,\mathrm{CISS} = 100 * (R_N - R_S)/(R_N + R_S)$ (*A*) Dependence of CISS on the type of electrode, measured by IS under 60% RH and constant magnetic field. (*B*) Humidity dependence of CISS for Ni/Ni electrodes under constant magnetic field, measured by IS across a range of RH levels, see also *SI Appendix*, Fig. S3 for averaged resistance values. A similar effect was seen for DC measurements (*SI Appendix*, Fig. S4). (*C*) Effect of the humidity source on CISS, comparing H_2O and D_2O at 60% RH with Ni electrodes and under constant magnetic field, measured by IS. The average resistance values compared between H_2O and D_2O are presented in *SI Appendix*, Fig. S8. (*D*) Temperature dependence of CISS, measured by DC IV measurements at 70% RH with Ni electrodes. Panels (*A*–*C*) are derived from IS measurements, while panel (*D*) is based on DC IV measurements.

2nd harmonic signal under heating were compared for the two-spin injection.

The clear second harmonic peak observed in the AC current signal indicates the nonlinear nature of the conduction (55, 56), consistent with the involvement of phonons in the process (57, 58). The more pronounced second harmonic peak observed with laser heating (Fig. 4*B*) supports the role of phonons in the conduction mechanism, consistent with phonon-mediated electron–proton coupling (59). The dependence of the second harmonic signal on the magnetization direction (Fig. 4*C*) relates the heating and proton transport to electron spin polarization, consistent with phonon-mediated electron–proton coupling (59). The proton current profile is sensitive to the local heating and the injected electron spin. These results highlight the influence of the injected spin on phonon-mediated conduction.

Discussion

It is accepted that protons move through a medium by hopping between neighboring water molecules or other suitable carriers. Protons primarily carry the conduction current in lysozyme, sustained by coupling with electron flow. The gradual current decay over time (*SI Appendix*, Fig. S9) reflects the limits of proton transport, leading to eventual saturation. The energy of the protonation–deprotonation process is governed by the electrostatic potential generated by the proton electrochemical gradient and the intrinsic pKa values of the system.

In many cases, including biological systems such as in respiratory and photosynthetic complexes, electron and proton conduction are interconnected, playing vital roles in energy transfer and chemical reactions (60). Here, we provide evidence for proton-coupled electron transfer (PCET) mechanism in Lysozyme crystals by demonstrating that the proton transfer rate depends on the spin of the injected electrons. It is also demonstrated here that spin polarization affects the conductance at different temperatures and humidity conditions in the lysozyme crystals due to the coupling between spin polarization and chiral phonons (29, 61).

A sketch of the suggested model is presented in Fig. 5. We propose that proton transfer in the crystal generates electron polarization. The polarized electrons have a specific spin due to the chiral environment. The spin-polarized electrons interact with phonons during the proton transfer process, increasing the local temperature. This effect is enhanced by chiral phonons that are critical in preserving angular momentum. In chiral systems, these phonons can be chiral with a preference to specific chirality, and therefore, the phonons can carry angular momentum (29).

Another possible explanation for the observed mechanism is hydrogen atom transfer (HAT), a specific case of PCET, in which both a proton and its associated electron are transferred together (62–65). In a chiral environment, such as lysozyme crystals, chiral water wires could form (66), potentially facilitating long-range charge transport through coupled proton and electron motion. This mechanism aligns with theoretical studies suggesting that water-mediated HAT can contribute to efficient charge transport in biological and enzymatic systems (42, 67, 68). HAT could be regarded as a specific case of the PCET we discuss, where the electron and proton move together along the same pathway.

The HAT mechanism does not require a third particle (phonon) to explain the phenomenon. However, it does require the presence of specific amino acids that can participate in HAT, such as tyrosine, cysteine, tryptophan, and possibly histidine. Temperature dependence measurements, 2nd harmonic measurements (Fig. 4), as well as the new nonlinearity in the IV (*SI Appendix*, Fig. S11), may point to the involvement of phonons in the process.

As a control, we used Au electrodes that inject electrons having both spin states. Indeed, in this case, the observed CISS effect of proton conductivity in the chiral system is reduced, showing that the observed CISS effect is correlated with the spin polarization of injected electrons. The proposed transport mechanism is also supported by the observed differences in conductivity at different humidity. In D_2O environment, the CISS effect is lower than in H_2O environment, a phenomenon that can be related to lower coupling to phonons at the relevant energies. When the crystal becomes softer because of an increase in water content in the crystal, the interactions with the chiral environment are reduced and so does the CISS effect.

Notably, the observed CISS effect is due to changes to the proton transfer rate and hence the proton mobility (Fig. 2*B*). This observed change in the relaxation time is supported by a simplified

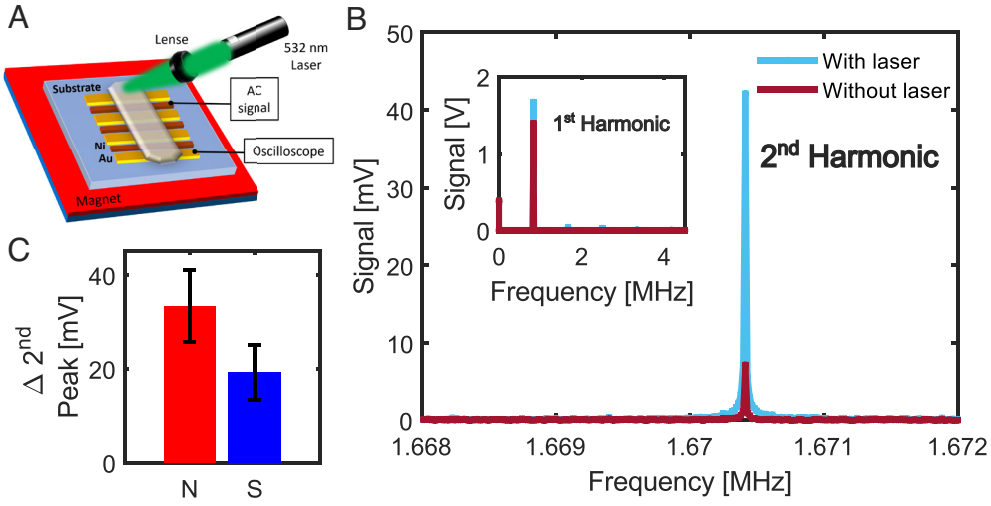

Fig. 4. Second harmonic measurements. (*A*) Schematic illustration of the measurement setup. Laser is focused on one side of the crystal, generating a temperature gradient across the crystal. AC voltage is applied, and the current signal is recorded by an oscilloscope. (*B*) Second harmonic peak and fundamental peak (*Inset*) of the AC signal, measured under a North magnetic field configuration, averaged over 30 measurements. A similar measurement was done for the south magnetic field, see *SI Appendix*, Fig. S6. (*C*) Difference in the second harmonic peak (Δ2nd Peak) with and without laser heating, comparing North and South magnetization directions, averaged over five measurement sets with 30 repetitions each. This surprising difference connects the spin electron spin polarization to phonons and to proton transfer.

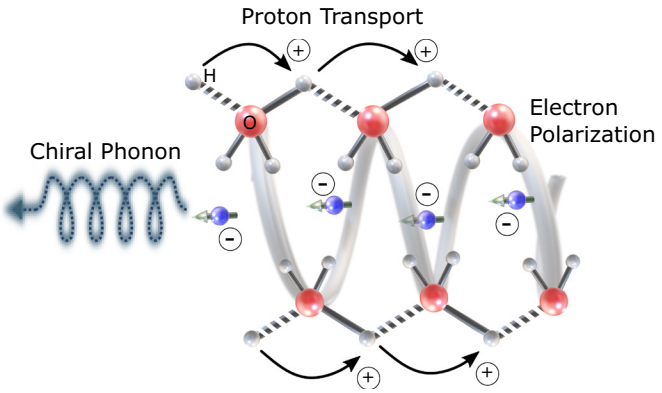

Fig. 5. A schematic proton transport toy model. The proton transport is accompanied by electron polarization. In chiral media, due to the CISS effect, this electric polarization is producing spin polarization. Preserving angular momentum generates chiral phonons that induce spin-selective proton transfer.

model of the Nyquist plots that have very common features found in many IS data (69). To characterize the magnetic field dependence, we describe this model within the equivalent circuit, describing the impedance data are composed of a Warburg element in series with a resistance R and a capacitance C in a parallel combination that defines a time constant $\tau = RC$. The impedance Z is normalized to a resistance R_u and the pulsation ω to a reference pulsation $\omega_u = 1/\tau_u$. Thus, the normalized impedance is given by,

$$Z_n = R_n \frac{1 - j\omega_n\tau_n}{1 + {\omega_n}^2{\tau_n}^2} + \frac{\rho_n}{\sqrt{\omega_n}} \frac{1 - \beta j}{\sqrt{1 + \beta^2}}, \qquad [1]$$

The Nyquist plots generated according to Eq. **1** (*SI Appendix*, Fig. S2) match the data of Fig. 2*A*. The resistance and the time constant were chosen so that the capacitance $C_n = \tau_n/R_n$ stays the same. This corresponds to the assumption that the dielectric properties of the crystal do not change when a magnetic field is applied. The Warburg parameter β of 2 is often observed when using porous electrodes (70). Comparison of *SI Appendix*, Fig. S2 and Fig. 2 implies that the resistance $R_u \approx 1.4$ MOhm. The *Inset* of *SI Appendix*, Fig. S2 allows us to estimate that $\omega_u \approx 200$ MHz ($\omega = \omega_n\omega_u$). The Warburg coefficient ρ_n was adjusted so that the phase data peaked at the same value as the data. The large difference between τ_n for the different magnetization conditions shows that the proton transport strongly depends on the electronic spin injection.

The relation between heat and phonon transfer on the one hand, and the electron spin on the other hand, is evidenced by the nonuniform laser heating of the crystal that triggers a second harmonic generation, practically only in the case when the North magnetization is applied (Fig. 4).

Conclusions

The present work highlights the intricate relationship between electron and proton transport. Since proton transfer in life typically occurs through chiral systems, like proteins and membranes, the electrons that are coupled to proton transfer are spin polarized. Spin polarization, besides enabling efficient electron transfer, also causes chiral phonon excitation that influences the proton transfer rate in a spin-selective manner. The present study supports the PCET mechanism in lysozyme crystals and provides insight into the mechanism of proton transfer in these crystals. In that picture, the electron generates a polarization wave that accompanies the proton transfer, changing the proton effective mass. The results emphasize the role of chirality in biological processes. These findings bridge quantum physics with biochemistry, enabling a better understanding and controlling information transfer in the biological environment.

Methods

Lysozyme Crystallization. Tetragonal lysozyme crystals were obtained utilizing the hanging-drop vapor-diffusion method (44, 71). In particular, Hen egg white lysozyme tends to crystallize easily in a tetragonal space group symmetry [$a = 76.5$ Å, $c = 37.0$ Å]. This crystal form has a Mathews Coefficient value (V_M) of 1.85 Å^3/Da with a corresponding solvent content of 33.7%. A 6 μL drop, comprising equal volumes of protein solution (30 to 46 mg/mL in 100 mM NaAcetate, pH 4.8) and reservoir solution (1 M NaCl, 0.1 M sodium acetate, pH 4.2), was employed. Prior to cross-linking, the crystals underwent three washes with reservoir solutions to eliminate noncrystallized lysozymes. For cross-linking, the crystals were immersed in a solution containing 5% glutaraldehyde in 1 M NaCl, 0.1 M NaAcetate, pH 4.2. After an incubation period of 24 to 30 h, the crystals were retrieved and transferred to distilled deionized water. The size of a single crystal is approximately 300 μm in each dimension. An image via scanning electron microscopy (SEM) is shown in Fig. 1*A* and *SI Appendix*, Fig. S1. Hen egg white lysozyme, used in these experiments, is regularly purchased commercially and is in a high grade of purity and no further purification protocol is required. Tetragonal lysozyme crystals are being analyzed at X-ray facilities (mainly ESRF, Grenoble, France) and their three-dimensional structure solved to substantiate its characteristics. The crystal preparation procedure follows that described in ref. 71, and the X-ray scattering analysis performed at ESRF (for crosslinked at pH 4.8) corresponds to the crystals used in our study.

Device Preparation. A Si/SiO_2 substrate was used as the base for device fabrication. Standard photolithographic techniques were employed to pattern electrodes, followed by metal evaporation and lift-off procedures. Four gold electrodes (10 nm Ti and 50 nm Au) and three nickel electrodes (50 nm Ni and 10 nm Au) were deposited alternately, with electrode widths ranging from 2 μm for the Ni electrodes to 5 μm for the Au electrodes. Spacing between electrodes was approximately 2 μm. Subsequently, a single lysozyme crystal was manually positioned on the device. Fig. 1*B* shows the device schematic, and Fig. 1*C* shows the lysozyme crystal situated on Ni and Au electrodes, as used for impedance and IV measurements.

An 80 mT field strength was used to magnetize the Ni. The field was determined by directly measuring the magnetization of the Ni sample using a gaussmeter, positioned at the same distance from the magnet as the sample in our experiments. Additionally, vibrating sample magnetometry measurements were performed on the substrates showing a coercive field of about 25 mT. This is shown in *SI Appendix*, Fig. S13.

Electrical Characterizations. DC IV measurements were done on a bondage sample with standard two-probe configuration.

Impedance measurements were performed in a probe station (ST-500, Janis, USA) using a frequency response analyzer and a dielectric interface (1260b and 1296, Solartron Metrology, UK). Spectra were recorded over a frequency range of 32 to 3.2 MHz, using AC voltage with an amplitude of 100 mV. The spectra were recorded for four Ni–Ni devices, three Au–Au devices, and two Ni–Au devices under N, S, and WO magnetization in 60 to 80% RH range at room temperature. Measurements were performed using both H_2O and D_2O, to test for the kinetic isotope effect. The collected impedance data were fitted with an equivalent circuit model using the EC lab software to extract the resistance. The charge carrier relaxation time was extracted from the frequency of the maximal loss tangent values.

Second Harmonic Measurements. An AC 0.1 V voltage of 850 kHz was applied to the crystal placed on Au–Ni electrodes, and the current response was measured by recording 100,000 data points using an oscilloscope. The fundamental peak of the signal and the second harmonic peak are shown in Fig. 4*B*. A 532 nm green laser of 5 mW was focused by a lens on the crystal side to locally heat the sample. The laser was calibrated on a thermal resistor, confirming that it induced a temperature increase of approximately 1 to 2 °C. Experiments were

performed in a high-humidity environment of about 80% RH, with a constant magnet placed beneath the sample as before. Measurements were conducted in different magnetization directions (North and South), both with and without the laser to assess the effect of local heating. Each configuration was measured 30 times and analyzed using Fast Fourier Transform, with each magnetization configuration repeated five times for consistency.

Data, Materials, and Software Availability. All study data are included in the article and/or *SI Appendix*.

ACKNOWLEDGMENTS. Air Force FA8655-24-1-7390, German Research Foundation – the Deutsche Forschungsgemeinschaft, TRR-386, project number 514664767.

Author affiliations: [a]Department of Applied Physics, Center for nanoscience and Nanotechnology, Hebrew University of Jerusalem, Jerusalem 9190401, Israel; [b]Department of Materials Engineering, Ilse Katz Institute for Nanoscale Science and Technology, Ben-Gurion University of the Negev, Beer-Sheva 84105, Israel; [c]The Wolfson Centre for Applied Structural Biology, Department of Biological Chemistry, Alexander Silverman Institute of Life Sciences, The Edmond J. Safra Campus, The Hebrew University of Jerusalem, Jerusalem 91904, Israel; [d]Department of Plant and Environmental Sciences, Edmond J. Safra Campus, The Alexander Silberman Institute of Life Sciences, Hebrew University of Jerusalem, Givat Ram, Jerusalem 9190402, Israel; [e]Institute of Physics, Ecole Polytechnique Fédérale de Lausanne, Lausanne 1015, Switzerland; and [f]Department of Chemical and Biological Physics, Weizmann Institute, Rehovot 76100, Israel

Author contributions: N.G., P.P., S.Y., N.A., and Y.P. designed research; Y.E.-D. and O.L prepared the crystals; N.G. prepared the devices; N.G., P.P., and N.A. performed measurements; N.G., J.-P.A., and N.A. contributed new reagents/analytic tools; N.G., P.P., J.-P.A., and N.A. analyzed data; and N.G., P.P., Y.E.-D., S.Y., N.K., J.-P.A., R.N., O.L., N.A., and Y.P. wrote the paper.

1. P. Mitchell, Coupling of phosphorylation to electron and hydrogen transfer by a chemi-osmotic type of mechanism. *Nature* **191**, 144–148 (1961).
2. Z. Schulten, K. Schulten, "[30] Proton conduction through proteins: An overview of theoretical principles and applications" in *Methods in Enzymology*, L. Packer, Ed. (Academic Press, 1986), vol. 127, pp. 419–438.
3. K.-D. Kreuer, Proton conductivity: Materials and applications. *Chem. Mater.* **8**, 610–641 (1996).
4. A. T. Jagendorf, Chance, luck and photosynthesis research: An inside story. *Photosynth. Res.* **57**, 215–229 (1998).
5. T. E. Decoursey, Voltage-gated proton channels and other proton transfer pathways. *Physiol. Rev.* **83**, 475–579 (2003).
6. V. R. I. Kaila, M. Wikström, G. Hummer, Electrostatics, hydration, and proton transfer dynamics in the membrane domain of respiratory complex I. *Proc. Natl. Acad. Sci. U.S.A.* **111**, 6988–6993 (2014).
7. W. Junge, N. Nelson, ATP synthase. *Annu. Rev. Biochem.* **84**, 631–657 (2015).
8. J. F. Nagle, S. Tristram-Nagle, Hydrogen bonded chain mechanisms for proton conduction and proton pumping. *J. Membrain Biol.* **74**, 1–14 (1983).
9. A. Y. Mulkidjanian, J. Heberle, D. A. Cherepanov, Protons @ interfaces: Implications for biological energy conversion. *Biochim. Biophys. Acta* **1757**, 913–930 (2006).
10. P. R. Rich, A. Maréchal, Functions of the hydrophilic channels in protonmotive cytochrome c oxidase. *J. R. Soc. Interface* **10**, 20130183 (2013).
11. L I. Krishtalik, The mechanism of the proton transfer: An outline. *Biochim. Biophys. Acta* **1458**, 6–27 (2000).
12. J. F. Nagle, M. Mille, H. J. Morowitz, Theory of hydrogen bonded chains in bioenergetics. *J. Chem. Phys.* **72**, 3959–3971 (1980).
13. D. V. Matyushov, M. D. Newton, Electron-induced proton transfer. *J. Phys. Chem. B* **125**, 12264–12273 (2021), 10.1021/acs.jpcb.1c06949.
14. R. Hempelmann, Diffusion of hydrogen in metals. *J. Less Common Metals* **101**, 69–96 (1984).
15. A. Braun, Q. Chen, Experimental neutron scattering evidence for proton polaron in hydrated metal oxide proton conductors. *Nat. Commun.* **8**, 15830 (2017).
16. F. Fontaine-Vive, M. R. Johnson, G. J. Kearley, J. A. K. Howard, S. F. Parker, How phonons govern the behavior of short, strong hydrogen bonds in urea—phosphoric acid. *J. Am. Chem. Soc.* **128**, 2963–2969 (2006).
17. A. Migliore, N. F. Polizzi, M. J. Therien, D. N. Beratan, Biochemistry and theory of proton-coupled electron transfer. *Chem. Rev.* **114**, 3381–3465 (2014).
18. K. Wakamura, Ion conduction in proton- and related defect (super) ionic conductors: Mechanical, electronic and structure parameters. *Solid State Ionics* **180**, 1343–1349 (2009).
19. K. Wakamura, Roles of phonon amplitude and low-energy optical phonons on superionic conduction. *Phys. Rev. B* **56**, 11593–11599 (1997).
20. S. Hammes-Schiffer, A. A. Stuchebrukhov, Theory of coupled electron and proton transfer reactions. *Chem. Rev.* **110**, 6939–6960 (2010).
21. Y. Chalopin, S. P. Cramer, S. Arragain, Phonon-assisted electron–proton transfer in [FeFe] hydrogenases: Topological role of clusters. *Biophys. J.* **122**, 1557–1567 (2023).
22. M. H. V. Huynh, T. J. Meyer, Proton-coupled electron transfer. *Chem. Rev.* **107**, 5004–5064 (2007).
23. B. P. Bloom, Y. Paltiel, R. Naaman, D. H. Waldeck, Chiral induced spin selectivity. *Chem. Rev.* **124**, 1950–1991 (2024).
24. R. Naaman, D. H. Waldeck, Chiral-induced spin selectivity effect. *J. Phys. Chem. Lett.* **3**, 2178–2187 (2012).
25. L. Zhang, Q. Niu, Chiral phonons at high-symmetry points in monolayer hexagonal lattices. *Phys. Rev. Lett.* **115**, 115502 (2015).
26. M. Weißenhofer *et al.*, Truly chiral phonons arising from chirality-selective magnon-phonon coupling. *Synthical* (2024). https://synthical.com/article/Truly-Chiral-Phonons-Arising-From-Chirality-Selective-Magnon-Phonon-Coupling-9cd2bbbb-7719-4d40-a6c9-a8b9d048b4d9.
27. G.-F. Du, H.-H. Fu, R. Wu, Vibration-enhanced spin-selective transport of electrons in the DNA double helix. *Phys. Rev. B* **102**, 035431 (2020).
28. K. Kim *et al.*, Chiral-phonon-activated spin Seebeck effect. *Nat. Mater.* **22**, 322–328 (2023).
29. J. Fransson, Chiral phonon induced spin polarization. *Phys. Rev. Res.* **5**, L022039 (2023).
30. P. T. Henderson, D. Jones, G. Hampikian, Y. Kan, G. B. Schuster, Long-distance charge transport in duplex DNA: The phonon-assisted polaron-like hopping mechanism. *Proc. Natl. Acad. Sci. U.S.A.* **96**, 8353–8358 (1999).
31. S.-H. Yang, R. Naaman, Y. Paltiel, S. S. P. Parkin, Chiral spintronics. *Nat. Rev. Phys.* **3**, 328–343 (2021).
32. O. Ben Dor *et al.*, Magnetization switching in ferromagnets by adsorbed chiral molecules without current or external magnetic field. *Nat. Commun.* **8**, 14567 (2017).
33. N. Goren *et al.*, Metal organic spin transistor. *Nano Lett.* **21**, 8657–8663 (2021).
34. C. C. F. Blake *et al.*, Structure of hen egg-white lysozyme: A three-dimensional Fourier synthesis at 2 Å resolution. *Nature* **206**, 757–761 (1965).
35. A. Yonath, A. Sielecki, J. Moult, A. Podjarny, W. Traub, Crystallographic studies of protein denaturation of renaturation. 1. Effects of denaturants on volume and x-ray pattern of crosslinked triclinic lysozyme crystals. *Biochemistry* **16**, 1413–1417 (1977).
36. M. A. Hossain *et al.*, Efficient transfer of chirality in complex hybrid materials and impact on chirality-induced spin selectivity. *Chem. Mater.* **36**, 11449–11461 (2024).
37. S. Bone, Proton pathways in lysozyme. *Biochim. Biophys. Acta* **1078**, 336–338 (1991).
38. H. Morgan, R. Pethig, Protonic and ionic conduction in lysozyme. Hydration and field-dependent effects. *J. Chem. Soc., Faraday Trans.* **82**, 143–156 (1986).
39. M. Ataka, S. Tanaka, Electrical conductivity of single crystals of lysozyme. *Biopolymers* **19**, 669–679 (1980).
40. D. D. Eley, D. I. Spivey, The semiconductivity of organic substances. Part 6—A range of proteins. *Trans. Faraday Soc.* **56**, 1432–1442 (1960).
41. P. Ferraboschi, S. Ciceri, P. Grisenti, Applications of lysozyme, an innate immune defense factor, as an alternative antibiotic. *Antibiotics* **10**, 1534 (2021).
42. H. G. Nagendra, N. Sukumar, M. Vijayan, Role of water in plasticity, stability, and action of proteins: The crystal structures of lysozyme at very low levels of hydration. *Proteins* **32**, 229–240 (1998).
43. M. Madhusudan, M. Vijayan, Rigid and flexible regions in lysozyme and the invariant features in its hydration shell. *Curr. Sci.* **60**, 165–170 (1991).
44. E.-K. Yan *et al.*, Preparation of cross-linked hen-egg white lysozyme crystals free of cracks. *Sci. Rep.* **6**, 34770 (2016).
45. T. Nakanishi *et al.*, Observation of proton transfer coupled spin transition and trapping of photoinduced metastable proton transfer state in an Fe(II) complex. *J. Am. Chem. Soc.* **141**, 14384–14393 (2019).
46. R. de Levie, The electrolysis of water. *J. Electroanal. Chem.* **476**, 92–93 (1999).
47. S. Ma *et al.*, Magnetic field-assisted water splitting: Mechanism, optimization strategies, and future perspectives. *Adv. Funct. Mater.* **34**, 2316544 (2024).
48. S. Censor *et al.*, Long-range proton channels constructed via hierarchical peptide self-assembly. *Adv. Mater.* **36**, 2409248 (2024).
49. A. Javed, T. Wagner, S. Wöhlbrandt, N. Stock, M. Tiemann, Proton conduction in a single crystal of a phosphonato-sulfonate-based coordination polymer: Mechanistic insight. *ChemPhysChem* **21**, 605–609 (2020).
50. S. J. Edwards, A. V. Soudackov, S. Hammes-Schiffer, Analysis of kinetic isotope effects for proton-coupled electron transfer reactions. *J. Phys. Chem. A* **113**, 2117–2126 (2009).
51. À. González-Lafont, J. M. Lluch, Kinetic isotope effects in chemical and biochemical reactions: Physical basis and theoretical methods of calculation. *WIREs Comput. Mol. Sci.* **6**, 584–603 (2016).
52. M. K. Gupta *et al.*, Phonons and anomalous thermal expansion behaviour of H2O and D2O ice Ih. *Phys. Rev. B* **98**, 104301 (2018).
53. L. De Marco *et al.*, Differences in the vibrational dynamics of H2O and D2O: Observation of symmetric and antisymmetric stretching vibrations in heavy water. *J. Phys. Chem. Lett.* **7**, 1769–1774 (2016).
54. T. K. Das, F. Tassinari, R. Naaman, J. Fransson, Temperature-dependent chiral-induced spin selectivity effect: Experiments and theory. *J. Phys. Chem. C* **126**, 3257–3264 (2022).
55. R. Tirole *et al.*, Second harmonic generation at a time-varying interface. *Nat. Commun.* **15**, 7752 (2024).
56. C. Wang, D. Gao, L. Gao, Detecting nonlocality by second-harmonic generation from a graphene-wrapped nanoparticle. *Opt. Express* **30**, 12722–12731 (2022).
57. A. Bojahr *et al.*, Second harmonic generation of nanoscale phonon wave packets. *Phys. Rev. Lett.* **115**, 195502 (2015).
58. M. Först *et al.*, Nonlinear phononics as an ultrafast route to lattice control. *Nat. Phys.* **7**, 854–856 (2011).
59. T. K. Paul, S. Taraphder, Nonlinear reaction coordinate of an enzyme catalyzed proton transfer reaction. *J. Phys. Chem. B* **126**, 1413–1425 (2022).
60. A. Migliore, N. F. Polizzi, M. J. Therien, D. N. Beratan, Biochemistry and theory of proton-coupled electron transfer. *Chem. Rev.* **114**, 3381–465 (2014), 10.1021/cr4006654.
61. H. Zhu *et al.*, Observation of chiral phonons. *Science* **359**, 579–582 (2018).
62. J. M. Mayer, Understanding hydrogen atom transfer: From bond strengths to Marcus theory. *Acc. Chem. Res.* **44**, 36–46 (2011).
63. J. Silverman, R. W. Dodson, The exchange reaction between the two oxidation states of iron in acid solution. *J. Phys. Chem.* **56**, 846–852 (1952).
64. J. Hudis, R. W. Dodson, Rate of ferrous-ferric exchange in D2O1. *J. Am. Chem. Soc.* **78**, 911–913 (1956).
65. J. T. Hupp, M. J. Weaver, Electrochemical and homogeneous exchange kinetics for transition-metal aqua couples: Anomalous behavior of hexaaquairon(III/II). *Inorg. Chem.* **22**, 2557–2564 (1983).
66. I. Kocsis *et al.*, Oriented chiral water wires in artificial transmembrane channels. *Sci. Adv.* **4**, eaao5603 (2018).
67. D. J. Cárdenas, J. M. Cuerva, M. Alías, E. Buñuel, A. G. Campaña, Water-based hydrogen-atom wires as mediators in long-range proton-coupled electron transfer in enzymes: A new twist on water reactivity. *Chemistry* **17**, 8318–8323 (2011).
68. M. Wang, J. Gao, P. Müller, B. Giese, Electron transfer in peptides with cysteine and methionine as relay amino acids. *Angew. Chem. Int. Ed. Engl.* **48**, 4232–4234 (2009).
69. A. Lasia, *Electrochemical Impedance Spectroscopy and Its Applications* (Springer, New York, NY, 2014), 10.1007/978-1-4614-8933-7.
70. J. S. Newman, *Electrochemical Systems* (John Wiley & Sons, Hoboken, NJ, 2004).
71. Y. Wine, N. Cohen-Hadar, A. Freeman, F. Frolow, Elucidation of the mechanism and end products of glutaraldehyde crosslinking reaction by X-ray structure analysis. *Biotechnol. Bioeng.* **98**, 711–718 (2007).